Spin- and fine-structure-resolved ionization of krypton

S. Bellm,[1] J. Lower,[1] R. P. McEachran,[1] E. Weigold,[1] C. Ryan-Anderson,[2] and D. H. Madison[2]
[1]*AMPL, Research School of Physics and Engineering, The Australian National University, Canberra, ACT 0200, Australia*
[2]*Missouri University of Science and Technology, 1315 N. Pine Street, Rolla, Missouri 65409-0640, USA*
(Received 10 September 2008; published 10 December 2008)

The influence of exchange, correlation, and relativistic effects in the ionization of heavy-target atoms can be sensitively probed by kinematically complete studies involving spin-polarized electrons, in particular when the fine structure of the residual ion is resolved. We present spin asymmetries, triple differential cross sections, and branching ratios for the ionization, by 127.5-eV and 114.3-eV electrons, of ground-state krypton atoms leading to the Kr^+ $4s\ ^2S_{1/2}$, $4p^5\ ^2P_{1/2}$, and $4p^5\ ^2P_{3/2}$ states. In order to untangle contributions from different physical effects, the experimental results are compared to those from distorted-wave Born approximation calculations (non- and semirelativistic) in which bound-state and continuum effects are treated in different ways. Additional insight is gained by comparing the present experimental and theoretical results to recent results on the *e*-Xe system, performed under similar kinematics, for which target relativistic effects play a more significant role.

DOI: 10.1103/PhysRevA.78.062707 PACS number(s): 34.80.Dp, 34.80.Nz

I. INTRODUCTION

A. Motivation

An accurate experimental and theoretical determination of cross sections for ionization induced by electron impact is desirable for a variety of reasons.

First, it is important for modeling the behavior of plasmas and ionized gases where many different collision processes are in competition. The accuracy to which the properties of these systems can be described depends on the quality of the cross-section data they incorporate. Applications include modeling the upper atmosphere, fusion reactors, lasers, radiation damage to biological material mediated through low-energy electron impact, and modeling candidates for new light sources to replace present mercury-based technologies.

Second, comparison of the cross sections derived from experiment with those derived by theory allows the underlying mechanisms for the interaction of charged particles with matter to be investigated and the predictive powers of theory to be refined. While it is known that quantum mechanics and relativity determine the reaction outcomes, high-accuracy calculations of atomic ionization cross sections within these frameworks often prove problematic. This is because, by their nature, such calculations are computationally intensive and the approximations they incorporate to render the problem tractable often lead to inaccuracies which are difficult to quantify. Therefore, a key issue is to determine the appropriateness and efficacy of the different approximate theoretical approaches under different kinematical conditions.

In order to provide the most stringent tests of theory, highly differential experimental cross-section data are the most desirable. This involves determining as many as possible of the kinematical and quantum mechanical variables which characterize the ionization process. By a judicious choice of reaction kinematics and through quantum-state selectivity of reactants and products, such data enable different aspects of the collision dynamics to be highlighted, and sometimes even isolated. To this end, we focus our present study on the so-called "triple differential cross sections" (TDCS) for which the momenta of the incoming and two outgoing electrons comprising each $(e,2e)$ ionization event are resolved. We achieve quantum-state selectivity by employing beams of spin-polarized electrons and energetically resolving the fine structure of the residual ion. In order to aid in the discussion of the reaction kinematics and the spin-related quantities pertinent to the present study, Fig. 1 shows a schematic representation of the $(e,2e)$ scattering geometry and the coordinate system we adopt to describe it.

For the present study, a quantity proportional to the TDCS is determined experimentally by the electron coincidence technique with electron momentum analyzers employed to determine the respective momenta ($\mathbf{p}_1$ and $\mathbf{p}_2$) and energies (E_1 and E_2) of the two continuum electrons comprising individual $(e,2e)$ events. When combined with a knowledge of the incident electron momentum $\mathbf{p}_0$ (energy E_0), the recoil momentum of the ion $\mathbf{q}$ and the binding energy ε of the

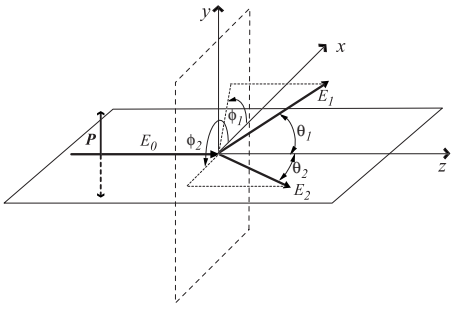

FIG. 1. Schematic representation of the scattering geometry and coordinate system defining the TDCS. An incident electron of energy E_0 (momentum $\mathbf{p}_0$) ionizes a target atom, resulting in the ejection of two electrons of respective energies (momenta) E_1 ($\mathbf{p}_1$) and E_2 ($\mathbf{p}_2$) into the polar and azimuthal angles θ_1, θ_2 and ϕ_1, ϕ_2, respectively. For the condition $\phi_1=0$, $\phi_2=180°$ (coplanar geometry) the momentum vectors $\mathbf{p}_0$, $\mathbf{p}_1$, and $\mathbf{p}_2$ share a common plane, the so-called "scattering plane," indicated in the figure by the parallelogram delineated by a solid line. The present measurements are performed under such coplanar geometry with TDCSs measured for the electron beam polarization $\boldsymbol{P}$ orientated out of (solid arrow) or into (dashed arrow) the scattering plane.

ejected target electron can be determined through energy and momentum conservation:

$$\mathbf{q} = \mathbf{p}_0 - \mathbf{p}_1 - \mathbf{p}_2, \tag{1}$$

$$\varepsilon = E_0 - E_1 - E_2. \tag{2}$$

The spin dependence of the TDCS is additionally investigated by inverting the orientation of the polarization $\boldsymbol{P}$ describing the incident electron beam with respect to the scattering plane (see Fig. 1 and associated caption).

The main aim of the present study is to elucidate details of the process of electron-impact-induced ionization of heavy atoms using the electron-krypton system as a test case. To facilitate this, highly state-specific measurements and calculations are performed. Specifically, we study the dependence of the TDCS on the spin projection of the primary electron beam and on the momenta of the two final-state continuum electrons liberated by each ionization event. Transitions from ground-state krypton atoms leading to the Kr^+ $4s4p^6\,{}^2S_{1/2}$ state (ε=27.5 eV) and the spin-orbit-split Kr^+ $4p^5\,{}^2P_{1/2}$ and $4p^5\,{}^2P_{3/2}$ fine-structure levels (ε=14.67 and 14.00 eV, respectively) are considered. We note that while TDCS measurements have been previously reported in literature for the electron-krypton system, none exhibit the degree of state specificity inherent to the present study, which is achieved through using polarized electrons and by simultaneously resolving the fine-structure levels of the residual ion. Recent and significant improvements to our $(e,2e)$ binding energy resolution allow us to clearly resolve the Kr^+ $4p^5$ fine-structure doublet, as is evident from Fig. 2. This figure shows binding energy spectra obtained by plotting coincidence counts against binding energy ε for transitions to the $^2P_{1/2}$ and $^2P_{3/2}$ fine-structure levels. The reaction kinematics is described in the figure caption. Spectra are presented for positive [panel (a)] and negative [panel (b)] orientations of the electron-beam polarization, measured with respect to the scattering plane. A comparison of the two panels shows the presence of a strong spin asymmetry for the particular kinematics adopted in the figure. Mathematical definitions for all spin-dependent quantities treated in this paper are presented in Sec. I C.

The present reaction kinematics were chosen to closely mimic those of recent analogous experiments on xenon atoms [1] in which transitions to the Xe^+ $5p^5\,{}^2P_{1/2}$ and $5p^5\,{}^2P_{3/2}$ fine-structure levels (binding energies 13.44 and 12.13 eV, respectively) were studied and discrepancies with theory were observed whose origin was unclear. For the electron-krypton system, relative to the electron-xenon system, the influence of relativity should be reduced due to the smaller atomic number Z (Z=36 relative to Z=54).

B. Background

It has been well established, both theoretically and experimentally, that nonzero spin-up-down asymmetries are observed for the elastic scattering and electron-impact excitation of closed-shell rare-gas atoms below the threshold for ionization [2]. For elastic scattering, finite values of the spin asymmetry arise exclusively from the spin-orbit interaction

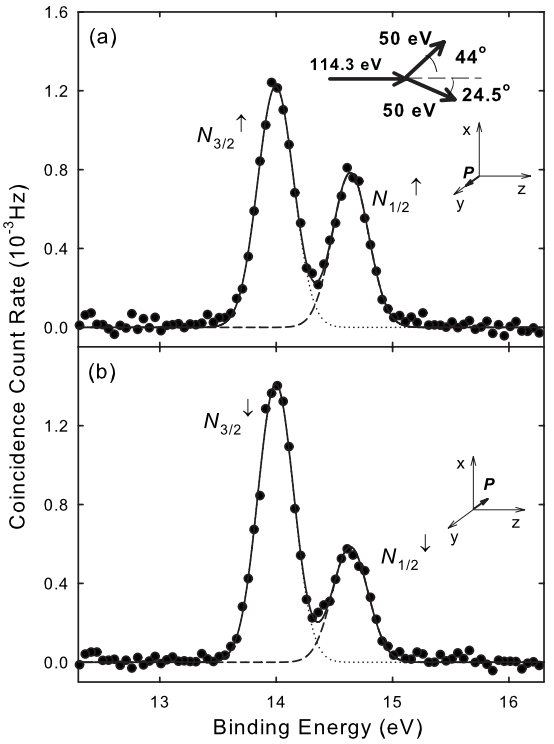

FIG. 2. Binding energy spectra showing transitions to the Kr^+ $4p^5\,{}^2P_{1/2}$ and $4p^5\,{}^2P_{3/2}$ states. The incident beam energy E_0 is 114.3 eV, and the average energies $\bar{E}_1$ and $\bar{E}_2$, respectively, of the two outgoing electrons are 50 eV. The measurement is performed under coplanar scattering geometry, with one electron detected to the left at an angle θ_1=44°, the second to the right at the angle θ_2=24.5°. The peaks are fitted with the instrument response function (dotted and dashed lines) to accurately extract count rates. Good agreement between the solid line (the envelope of the two fitted functions) and the experimental data illustrates the quality of the fit. $N_{1/2}^{\uparrow}$, $N_{3/2}^{\uparrow}$ and $N_{1/2}^{\downarrow}$, $N_{3/2}^{\downarrow}$ correspond, respectively, to the count rates for ionization by a positive [panel (a), $\boldsymbol{P}$ parallel to the y axis] and a negative [panel (b), $\boldsymbol{P}$ antiparallel to the y axis] primary electron-beam polarization. The differences in peak heights between spectra (a) and (b) reflect the presence of a strong spin asymmetry for these kinematics.

of the continuum electron in the field of the target atom (Mott scattering). For atomic excitation (including ionization), further contributions to the spin asymmetry may occur through an interplay of exchange scattering and the fine-structure interaction within the target when transitions to individual fine-structure levels are resolved. This occurs through a process referred to as the "fine-structure effect" [3–5]. While contributions to the spin-asymmetry function from the fine-structure effect remain finite in the nonrelativistic limit, those from Mott scattering do not. Thus for scattering from low-atomic-number (low-Z) atoms, nonnegligible contributions to the spin-asymmetry function are only expected through the fine-structure effect, while for heavy targets, significant contributions may occur through both the fine-structure effect and through Mott scattering.

For atomic excitation below the ionization threshold, the very good agreement between recent calculations by Bartschat and Zatsarinny [6] and the experimental work of Düm-

mler *et al.* [4] for argon and krypton targets suggests that electron-exchange scattering is the dominant mechanism underlying the observed asymmetries. However, for xenon the case is not clear as the results of Dümmler *et al.* [4] show strong violations from the predictions of a fine-structure-effect model which is applicable to atomic systems for which deviations from *LS* coupling are small (i.e., for systems in which bound-state relativistic effects are small).

For ionization studies of the noble gases (excluding the present work), experimental spin-resolved TDCS data, resolving fine-structure levels of the ion, have only been reported for xenon. This is because $(e,2e)$ coincidence experiments generally operate with a relatively poor binding energy resolution, typically 0.5–1.0 eV, in order to obtain sufficiently high count rates to render the experiments feasible. While such values of the resolution are sufficient to resolve (or partially resolve) the fine-structure levels of the valence p orbital of Xe^+ (1.3 eV separation), they are insufficient to resolve the corresponding levels for the lighter noble gases (e.g., 0.18 eV separation for argon, 0.097 eV for neon). Spin-asymmetry measurements for the e-Xe system have been previously reported by our group [1,7] and the group of Hanne [8,9]. Comparison of those results with the distorted-wave Born approximation (DWBA) calculations, calculated within a nonrelativistic framework, showed generally good agreement. This suggested that a nonrelativistic scattering theory might be adequate to describe the data. However, under some kinematics the agreement was less than satisfactory, leaving the question of whether contributions from continuum relativistic effects, not accounted for in the theory, were the cause for the disparities between the measured and calculated spin asymmetries. Our earlier study [10] showed that the employment of relativistic bound-state wave functions to describe the atom and the residual ion were necessary to accurately predict the branching ratio for transitions to the $J=1/2$ and $J=3/2$ ionic fine-structure levels. If continuum relativistic effects are *not* the cause for the persistent discrepancies between experiment and theory for the electron-xenon system, then other aspects of experimental and/or theoretical approaches must require refinement.

In order to try and resolve this issue, we present here a complementary study on krypton atoms under conditions where the energies of the scattered electrons are almost identical to those of our recent studies of xenon [1]. The motivation was to see if a reduced degree of disparity between experiment and scattering theory for the lower-Z krypton target could be achieved as well as to assess the size of contributions from relativity and to highlight potential areas of improvement in the theoretical treatment of electron scattering from heavy targets.

Experimentally, and in contrast to our earlier experimental work on xenon, we present here fully differential TDCS data for the electron-krypton system, in addition to spin asymmetries and branching ratios. The TDCS data, as we shall see, provide a much more sensitive test to certain aspects of the collision process.

On the theoretical side, we have refined our DWBA approach by performing a calculation employing relativistic scattering potentials in the determination of the continuum electron wave functions, thereby providing a partial account of continuum relativistic effects. In our previous xenon work [1] only nonrelativistic scattering potentials were used in the calculation of the continuum electron wave functions.

In detail the reactions considered here are

$$e^-(\boldsymbol{p}_0)(\uparrow\downarrow) + \mathrm{Kr}\ 4s^2 4p^6({}^1S_0) \rightarrow \mathrm{Kr}^+\ 4s^2 4p^5({}^2P_{1/2}, {}^2P_{3/2}) + e^-(\boldsymbol{p}_1) + e^-(\boldsymbol{p}_2), \quad (3)$$

$$e^-(\boldsymbol{p}_0)(\uparrow\downarrow) + \mathrm{Kr}\ 4s^2 4p^6({}^1S_0) \rightarrow \mathrm{Kr}^+\ 4s4p^6({}^2S_{1/2}) + e^-(\boldsymbol{p}_1) + e^-(\boldsymbol{p}_2). \quad (4)$$

Here, $\uparrow$ and $\downarrow$ represent, respectively, the positive and negative projections of the electron beam polarization with respect to the scattering plane. Note that while Eq. (3) concerns transitions to the fine-structure levels, Eq. (4) describes a transition to an S state for which no fine-structure exists. Thus, if any nonzero value of the spin asymmetry were to be observed for reaction (4), for which the fine-structure effect cannot contribute, it could only arise through Mott scattering.

Finally, to assist in assessing how the contributions from exchange scattering and relativity contribute to the present krypton data, additional fine-structure-resolved branching ratios are also presented for the scattering of *unpolarized* electrons from xenon atoms through the reaction

$$e^-(\boldsymbol{p}_0) + \mathrm{Xe}\ 5s^2 5p^6({}^2S_{1/2}) \rightarrow \mathrm{Xe}^+\ 5s^2 5p^5({}^2P_{1/2}, {}^2P_{3/2}) + e^-(\boldsymbol{p}_1) + e^-(\boldsymbol{p}_2). \quad (5)$$

These were not reported in our previous work [1].

Experimental TDCS studies of the $4p^6$ (and $4s^2$) valence shells of krypton have been performed previously by a number of groups for a range of reaction kinematics. They are reviewed briefly here. Of those $(e,2e)$ studies, none exhibited the degree of state specificity inherent to the present measurements, achieved by resolving the fine-structure levels of the ion accompanied by employing spin-polarized electrons.

Early experimental work on the valence structure of krypton [12,13], and more recently the work of Nicholson *et al.* [14], was performed under electron momentum spectroscopy [15] conditions under so-called noncoplanar symmetric reaction kinematics (i.e., high values of impact energy E_0, $E_1=E_2$, $\theta_1=\theta_2=45°$, $\phi_2=180°$, ϕ_1 varied in the neighborhood of 0°). Under such conditions where the scattering mechanism is greatly simplified, the momentum density of the target electrons at specific values of binding energy can be deduced from variations of the TDCS with the out-of-plane angle ϕ_1. These studies provided important tests to many-body descriptions of the krypton atom and residual ion. In contrast, the present work is performed at a much lower energy under coplanar energy-symmetric scattering geometry ($E_1=E_2$, $\phi_1=0$, $\phi_2=180°$, θ_1 and θ_2 varied). Under such kinematical conditions the scattering mechanism is much more complicated and the angular behavior of the TDCS is no longer determined solely by the momentum distribution of the target electrons.

Coplanar scattering geometry was employed by Selles *et al.* [16], who reported $(e,2e)$ measurements for energies

between 0.5 and 4.0 eV above threshold. The equal-energy-sharing conditions $E_1=E_2=0.25$, 0.5, 1.0, and 2 eV were adopted in their work. A total $(e,2e)$ binding energy resolution of ~300 meV enabled partial cross sections for transitions to the $4p^5\,{}^2P_{1/2}$ and $4p^5\,{}^2P_{3/2}$ fine-structure levels to be extracted. No calculations were presented to interpret this TDCS data.

In contrast to the symmetric-energy-sharing experiments described above, Rasch *et al.* [17] and Cavanagh *et al.* [18] performed studies under conditions of highly asymmetric energy-sharing ($E_1 \gg E_2$). Coplanar scattering geometry was employed in both cases.

Rasch *et al.* employed the scattered electron energies E_1 and E_2 of 1 keV and 20 eV, respectively, and performed measurements for scattering angles $1° < \theta_1 < 8°$. For Cavanagh *et al.*, E_1 and E_2 were 880 and 25 eV, respectively, and measurements were performed at the scattering angles $\theta_1=3°$, 5°, 8°, 10°, 15°, and 20°. Their data were placed on an absolute scale by normalizing to theoretical TDCSs for ionization of ground-state helium atoms and the results were compared to a DWBA calculation.

More recently, Williams *et al.* [19] performed measurements in the so-called "perpendicular-plane scattering geometry," for which the incident electron beam is directed along the normal of the scattering plane ($\theta_1=\theta_2=90°$). Equal-energy-sharing values of $E_1=E_2=2$, 1, 0.5, and 0.25 eV were employed in their studies, and partial cross sections were measured for transitions to the $4p^5\,{}^2P_{1/2}$ and $4p^5\,{}^2P_{3/2}$ fine-structure levels. The major characteristics of the TDCS were qualitatively explained by single- and double-scattering mechanisms. No calculations were presented to compare with their experimental results.

We also note the previous TDCS study of Haynes *et al.* [20] concerning the ionization of the 4*s* inner valence orbital of krypton, characterized by a binding energy of 27.5 eV, which is also a focus of the present work. Measurements were performed for the conditions of equal energy sharing $E_1=E_2=4$, 10, 20, 50, and 85 eV, and the experimental results were compared to DWBA calculations.

C. Definition of measured and derived parameters

To determine spin-resolved cross sections, one must perform measurements for an ensemble of ionization events, employing beams of spin-polarized electrons comprising an imbalance in the relative proportions of spin-up ($m_s=+1/2$) and spin-down ($m_s=-1/2$) electrons. For an ensemble of n electrons, the magnitude P of the spin polarization $\boldsymbol{P}$ is defined through the relation

$$P=\frac{n^{\uparrow}-n^{\downarrow}}{n^{\uparrow}+n^{\downarrow}}, \tag{6}$$

where $n^{\uparrow}$ is the number of electrons with spin projection $m_s=+1/2$ and $n^{\downarrow}$ is the number of electrons with spin projection $m_s=-1/2$. The main focus of this paper is the spin-asymmetry function. For a final angular momentum state J, it is defined by the expression

$$A_J(\theta_1,\theta_2)=\frac{\sigma_J^{\uparrow}-\sigma_J^{\downarrow}}{\sigma_J^{\uparrow}+\sigma_J^{\downarrow}}. \tag{7}$$

Here $\sigma_J^{\uparrow(\downarrow)}$ is the triple differential cross section for ionization by electrons of positive (negative) spin projection measured along the normal to the scattering plane. Experimentally, this quantity was determined by measuring the $(e,2e)$ count rates $N_J^{\uparrow}(\theta_1,\theta_2,P_y)$ and $N_J^{\downarrow}(\theta_1,\theta_2,P_y)$ for transitions leading to the final ion state J as a function of the scattering angles θ_1 and θ_2. P_y is the component of the spin polarization $\boldsymbol{P}$ of the electron beam measured along the normal to the scattering plane. For the present measurements, P_y was determined to be 0.42 ± 0.03 from measuring the up-down spin asymmetry in the elastic scattering of electrons from xenon at 50 eV [11]. The spin asymmetry $A_J(\theta_1,\theta_2)$ can then be derived through the expression [7]

$$A_J(\theta_1,\theta_2)=\frac{1}{P_y}\frac{N_J^{\uparrow}-N_J^{\downarrow}}{N_J^{\uparrow}+N_J^{\downarrow}}. \tag{8}$$

The spin-resolved TDCS $\sigma_J^{\uparrow(\downarrow)}$ is given by

$$\sigma_J^{\uparrow(\downarrow)}(\theta_1,\theta_2)=\frac{K}{P_y}[(1+P_y)N_J^{\uparrow(\downarrow)}-(1-P_y)N_J^{\downarrow(\uparrow)}]. \tag{9}$$

Here K is a constant (not determined by the present experiment) which depends on target-gas density, electron beam current, detector efficiencies, and other instrumental factors. In this paper we present the spin-averaged TDCS σ_J, given by

$$\sigma_J=KN_J. \tag{10}$$

Here the count rate N_J, $J=1/2$, $3/2$, is the average rate for unpolarized electrons and is calculated through the expression $N_J=(N_J^{\uparrow}+N_J^{\downarrow})/2$. K is obtained from a best visual fit of the experimental cross sections to theory.

Also presented are results, for both krypton and xenon, for the spin-averaged branching ratio $R(\theta_1,\theta_2)$, describing transitions to the $^2P_{1/2}$ and $^2P_{3/2}$ states and defined by the expression

$$R(\theta_1,\theta_2)=\sigma_{3/2}/\sigma_{1/2}=N_{3/2}/N_{1/2}. \tag{11}$$

In the nonrelativistic limit, based solely on the relative number of projection states m_J for the $^2P_{1/2}$ and $^2P_{3/2}$ states, a value of 2.0 is expected. As will be discussed, the fact that significant deviations from this value are observed in the present study, particularly for xenon, is a reflection of a significant influence of relativity on the radial behavior of the bound-state wave functions.

II. EXPERIMENT

A detailed description of the apparatus has been presented recently [23], so only a short account will be presented here. Polarized electrons are liberated by the photoexcitation of valence electrons from a strained gallium arsenide photocathode under illumination by circularly polarized laser light. These electrons are extracted, deflected through 90°, and focused to form a transversely polarized beam. The beam is

then transported to the collision chamber in which two toroidal-sector electrostatic electron energy analyzers are housed. In the collision chamber it is decelerated to the experimental collision energy E_0 via a new cylindrical seven-element electrostatic lens [24] and focused onto the krypton target beam, formed by the effusion of krypton gas through a 1.0-mm-internal-diameter tube orientated orthogonally to the scattering plane. Inversion of the beam polarization from out of (spin up) to into (spin down) the scattering plane is achieved by reversing the helicity of the laser light via a liquid crystal retarder.

Electrons emitted within the scattering plane are momentum analyzed in one of the two electron analyzers located on opposite sides of the projectile electron beam. Each analyzer comprises a seven-element annular-sector electrostatic lens system, four toroidal-sector electrodes, and a crossed-delay-line position-and-time-sensitive electron detector. The coordinates of energy and scattering angle (E_i, θ_i) for the detected electrons are deduced from their arrival coordinates (x_i, y_i) at the detector. $(e,2e)$ electron pairs are identified by the relative arrival times of electrons at the two detectors, with random background events subtracted using standard statistical techniques [25].

The energy E_0 of the projectile electron was stepped between two levels: 114.3 eV for the measurement of transitions to the Kr^+ $4p^5\ ^2P_{1/2}$ and $4p^5\ ^2P_{3/2}$ states and 127.5 eV for transitions to the Kr^+ $4s\ ^2S_{1/2}$ state. Over the course of the experiment this procedure was repeated many times to average over the effects of any instrumental drift, spending 20% of the total data collection time on the $4s$ transition and the remaining 80% on the $4p$ transitions.

Due to the difference in binding energies of the $^2P_{1/2}$ and $^2P_{3/2}$ states (14.67 and 14.00 eV, respectively), energy conservation, and the fixed-energy passbands for the two analyzers, the energy ranges for the measurements were as follows. For the $^2P_{3/2}$ state, data are collected for $(e,2e)$ events where $48.3\ \text{eV} < E_i < 52.0\ \text{eV}$, for the $^2P_{1/2}$ state, $48.0\ \text{eV} < E_i < 51.7\ \text{eV}$, and for the Kr^+ $4s\ ^2S_{1/2}$ state, $48.0\ \text{eV} < E_i < 52.0\ \text{eV}$, where $i=1,2$. Both electron detectors collect electrons over a 40° range simultaneously. One detector is fixed to collect electrons over the range $20° \leqslant \theta_1 \leqslant 60°$ on the left of the incident beam. The second detector, located on the right side of the incident beam, is movable and can collect electrons over a 40° band, adjustable from outside of the scattering chamber, within the angular limits $20° \leqslant \theta_2 \leqslant 120°$. For the present measurements, due to low coincidence rates at larger θ_2 values, data collection was restricted to $\theta_2 \leqslant 90°$.

The two analyzers were each operated with a 20-eV pass energy, leading to an energy resolution for each of around 200 meV full width at half maximum (FWHM). In combination with the intrinsic energy spread of the polarized electron beam of around 170 meV FWHM, an $(e,2e)$ binding energy resolution of 350 meV FWHM was achieved. This was sufficient to resolve the krypton fine-structure levels separated by 0.67 eV. However, to accurately determine the transition strength to each of the Kr^+ $4p^5\ ^2P_{1/2}$ and $4p^5\ ^2P_{3/2}$ fine-structure levels, they were fitted with the instrument response function to correct for their small degree (~5%) of intensity overlap (see Fig. 2). The instrument response function was determined by fitting the isolated peak, corresponding to transitions to the Kr^+ $4s$ state, by a single Gaussian of width adjusted for the best least-squares fit.

In order to improve the counting statistics, the TDCS and asymmetries were determined after performing an average of the $(e,2e)$ data over all combinations of E_1 and E_2 within the 4-eV acceptance bands of both analyzers. For an identical reason, an angular average over 4° intervals was performed in θ_1 and θ_2. The out-of-plane angular resolution of both toroidal analyzers was 1.4°.

We note that in contrast to our previous work on the electron-xenon system [1,7], we present here a much more extensive set of data for the electron-krypton system, including not only spin asymmetries, but also TDCS and branching ratio data.

III. THEORY

For the ionization of heavy atoms, the simplest viable theory is the distorted-wave Born approximation. Calculations performed within this framework generally provide a favorable degree of agreement with experiment at medium to high continuum electron energies. This is the approach we adopt in this paper to investigate the nature and magnitude of contributions from exchange scattering, correlation, and relativity, which, in combination with other effects, determine the behavior of the TDCSs.

As described in our previous publication [1], the description of electron-impact-induced ionization is complicated by two issues.

First, for atoms heavier than hydrogen, exchange occurs not only between the projectile and the ejected electrons, but also between the continuum electrons (the projectile electron in the initial state, the ejected and scattered electron in the final state) and all remaining bound electrons in the electron-atom system. The process of exchange between the continuum electrons and the atom and ion has been referred to as "exchange distortion" and is, in the DWBA formalism, treated in a distinctly different way than exchange between the projectile and ejected electron. Indeed, as shown in a previous study [21], this process can strongly contribute to the structure of the TDCS under certain conditions, as reflected in its influence on the calculated spin asymmetries. A proper treatment of many-body exchange processes requires the nonlocal character of exchange to be taken into account. Such a treatment was undertaken in our recent publication for the electron-xenon system [1] in which the Hartree-Fock method was used to calculate the continuum-electron wave functions within the DWBA formalism. However, a comparative theoretical study in that publication showed that accounting for exchange distortion approximately through the local exchange potential developed by Furness and McCarthy [22] was sufficient to account for many-body exchange effects under the kinematical conditions of that study. As the present study on the electron-krypton system is performed under kinematics that are nearly identical to that previous study, we adopt here the simpler approach of employing a local Furness-McCarthy (FM) exchange potential.

Second, the effects of relativity increase rapidly with increasing atomic number. While for low-Z atoms relativistic

effects in the electron-atom system can be accounted for through angular momentum coupling alone, for heavy atoms the influence of relativity on *both* the bound and continuum states should be taken into account.

The particular extension of the DWBA employed here, the so-called three-body distorted wave (3DW) approximation, has been described in previous publications [26,27], so only a brief overview will be presented here. The 3DW TDCS is obtained from

$$\frac{d^5\sigma}{d\Omega_a d\Omega_b dE_b} = \frac{1}{(2\pi)^5}\frac{k_a k_b}{k_i}(|T_{dir}|^2 + |T_{exch}|^2 + |T_{dir} - T_{exch}|^2), \tag{12}$$

where T_{dir} and T_{exch} are the direct and exchange amplitudes:

$$T_{dir} = S\langle \chi_a^-(\boldsymbol{r}_1)\chi_b^-(\boldsymbol{r}_2)C_{p\text{-}e}(|\boldsymbol{r}_1 - \boldsymbol{r}_2|)|V - U_i|\psi_i(\boldsymbol{r}_2)\chi_i^+(\boldsymbol{r}_1)\rangle, \tag{13}$$

$$T_{exch} = S\langle \chi_a^-(\boldsymbol{r}_2)\chi_b^-(\boldsymbol{r}_1)C_{p\text{-}e}(|\boldsymbol{r}_1 - \boldsymbol{r}_2|)|V - U_i|\psi_i(\boldsymbol{r}_2)\chi_i^+(\boldsymbol{r}_1)\rangle. \tag{14}$$

In Eqs. (13) and (14), $\boldsymbol{r}_1$ and $\boldsymbol{r}_2$ are the coordinates of the incident and bound electrons, respectively, χ_i, χ_a, and χ_b are the distorted waves for the incident, scattered, and ejected electrons, respectively, $\psi_i(\boldsymbol{r}_2)$ is the one-electron orbital of the active electron in the initial bound state, V is the Coulomb interaction between the projectile and the active electron, U_i is the initial-state spherically symmetric distorting potential which is used to calculate the initial-state distorted waves χ_i, and S is a spectroscopic factor. For the present study on krypton, S was taken as 0.98 for both the Kr^+ $4p^5\ ^2P_{1/2}$ and $4p^5\ ^2P_{3/2}$ fine-structure levels at 14.67 and 14.00 eV binding energies, respectively, and 0.51 for the $4s\ ^2S_{1/2}$ at 27.5 eV binding energy [14]. In addition, k_i, k_a, and k_b represent the magnitudes of the corresponding wave vectors $\boldsymbol{k}$, which are, in turn, related to their linear momenta via the relationship $\boldsymbol{p}=\hbar\boldsymbol{k}$. The $C_{p\text{-}e}$ term is the Coulomb interaction between the projectile and ejected electron, which allows for post-collision interaction (PCI). It is important to note that since this interaction is included in the final-state wave function, it is contained to all orders of perturbation theory. The normal first-order DWBA is obtained if $C_{p\text{-}e}=1$.

The Schrödinger equation for the incoming electron wave function is given by

$$\left(T + U_i - \frac{k_i^2}{2}\right)\chi_i^+(\boldsymbol{k}_i,\boldsymbol{r}) = 0, \tag{15}$$

where T is the kinetic energy operator and the "+" superscript on $\chi_i^+(\boldsymbol{k}_i,\boldsymbol{r})$ indicates outgoing wave boundary conditions. The initial-state distorting potential $U_i=U_s+U_e$, where U_s is the initial-state spherically symmetric static potential, and U_e is the FM [22] exchange potential which approximates the effect of the continuum electron exchanging with the passive bound electrons in the atom. We have previously shown that the FM potential is reasonably accurate for continuum electron energies of interest here [1].

The two final-channel distorted waves are obtained from a Schrödinger equation similar to Eq. (15):

$$\left(T + U_f - \frac{k_{a(b)}^2}{2}\right)\chi_{a(b)}^-(\boldsymbol{k}_{a(b)},\boldsymbol{r}) = 0. \tag{16}$$

Here the final-state distorting potential $U_f=U_{ion}+U_e$, where U_{ion} is the spherically symmetric static distorting potential for the atomic ion which is calculated using the same procedure as U_s, except that the active electron is removed from the charge distribution. The "−" superscript indicates boundary conditions for the incoming wave.

To gain deeper insight into the ionization process, DWBA calculations were performed at three distinct levels of approximation. In the first completely nonrelativistic calculation (labeled nrDWBA), the distortion potentials were determined from the Hartree-Fock orbitals of the ground-state wave function of the atom. Similarly, the one-electron orbital ψ_i of the active electron is the corresponding Hartree-Fock orbital. Two additional calculations were performed in order to partially investigate the effects of relativity and to investigate the effects of PCI on the ionization process. For these, the static Hartree-Fock potential U_s in the interaction potential U_i of the initial state was replaced by the corresponding relativistic Dirac-Fock potential. Similarly, the single Hartree-Fock static potential U_{ion} in the interaction potential U_f of the final state was replaced by the relativistic Dirac-Fock static potential of either the $^2P_{1/2}$ or $^2P_{3/2}$ ion. Finally, the one-electron Hartree-Fock orbital ψ_i of the active electron was replaced by the large component (renormalized to unity) of the corresponding one-electron Dirac-Fock orbital. This semirelativistic approach will be referred to as the srDWBA ($C_{p\text{-}e}=1$) or as the sr3DW when the PCI interaction is included.

IV. COMPARISON OF THEORY WITH EXPERIMENT

Figures 3 and 4 show the experimental TDCS data for transitions from ground-state krypton atoms to the Kr^+ $4p^5\ ^2P_{1/2}$ and $4p^5\ ^2P_{3/2}$ fine-structure levels, respectively. Figure 5 shows data for transitions to the Kr^+ $4s\ ^2S_{1/2}$ state. Error bars were calculated to take into account counting statistics and the estimated contribution from systematic errors which were difficult to correct for. The relative experimental TDCS data are compared to the three calculations described in Sec. III: namely, the nrDWBA, srDWBA, and sr3DW. The cross-normalized relative experimental data of Figs. 3–5 were placed on an absolute scale by normalizing to the sr3DW calculation at the coordinates $\theta_1=40°$, $\theta_2=52°$ in Fig. 3. These particular coordinate values were chosen to best facilitate a shape comparison between the experimental data and the srDWBA theory across all three figures. We emphasize here that only a single *common* normalization factor is required to place all of the experimental data of the three figures onto an absolute scale. Thus the present experimental data set, while not absolute, provides a stringent test of the presented calculations by assessing their ability to predict the relative intensities for transitions to three ionic final states (as well as testing their ability to predict the respective TDCS shapes) over a broad range of kinematics.

Focusing first on the experimental data and comparing Figs. 3 and 4, it is evident that the shapes of the angular

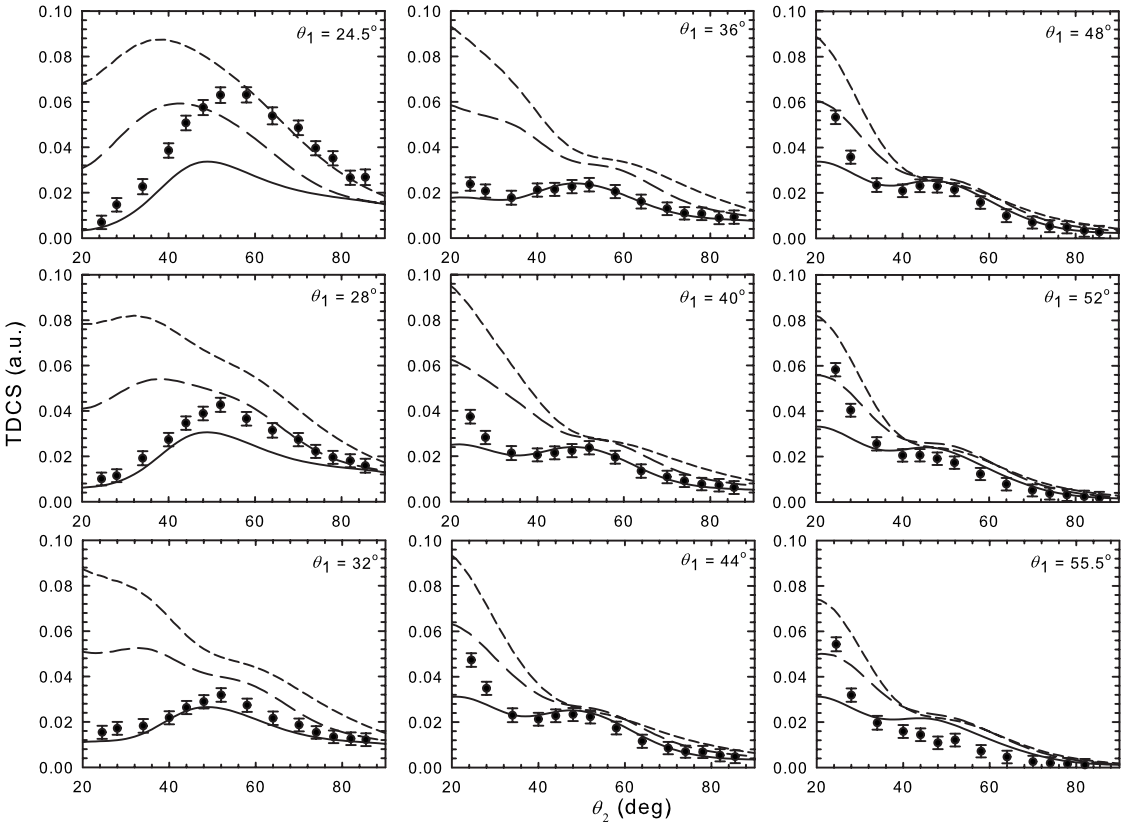

FIG. 3. TDCS for transitions to the Kr^+ $4p^5\,{}^2P_{1/2}$ ion state. The incident beam energy E_0 is 114.3 eV, and the average energies $\bar{E}_1$ and $\bar{E}_2$, respectively, of the two outgoing electrons are 49.9 eV. Theory: short-dashed line, nrDWBA; long-dashed line, srDWBA; solid line, sr3DW.

distributions for the two transitions are, to within error bars, identical, while the relative magnitudes of the two transitions differ by a factor of roughly 2.1. For both transitions the angular distributions show a double-peak structure. One peak is located around $\theta_2=52°$ and diminishes in magnitude as θ_1 increases. The second emerges as θ_1 increases at the angles $\theta_2 \leqslant 32°$. TDCSs for transitions to the Kr^+ $4s\,{}^2S_{1/2}$ state, shown in Fig. 5, show a similar angular behavior, although for this case one peak is located around $\theta_2=60°$. The other peak, emerging at small values of θ_2, is broader in this case and, with increasing values of θ_1, eventually becomes the sole peak in the spectrum as θ_2 is varied. The transition strength to this state is roughly 5 times smaller than for the combined strength for transitions to the individual Kr^+ $4p^5\,{}^2P_{1/2}$ and $4p^5\,{}^2P_{3/2}$ fine-structure levels.

Turning to the three calculations, the first thing to notice is the dramatic differences in predicted TDCS magnitude at small values of θ_2. As more physics is systematically incorporated into the calculations (as occurs through the progression from nrDWBA, srDWBA, through to the sr3DW calculation) the calculated cross section decreases in magnitude and exhibits improved shape agreement with experiment. Since the experimental data are not absolute, they cannot distinguish which of the three calculations predicts cross-section magnitudes closest to the true value. However, comparing the predicted shape of the respective angular distributions clearly shows that the more sophisticated the calculation, the better the agreement in shape with that of measurement.

As described earlier, the essential difference between the nrDWBA and srDWBA calculations is that the former uses nonrelativistic Hartree-Fock wave functions to describe the atomic and ionic bound states and to calculate the distorting potentials for the continuum electrons, whereas the latter uses Dirac-Fock wave functions to calculate the distorting potentials as well as renormalized Dirac-Fock wave functions to describe the active electron.

Clearly the predictions of the DWBA approach are extremely sensitive to the inclusion or exclusion of relativistic effects. In Figs. 3–5, the srDWBA provides a superior prediction of the position of the TDCS maximum at small values of θ_1 to its nonrelativistic counterpart, although neither predict the extremely rapid falloff in TDCS intensity as the angle θ_2 decreases to 20°.

The sr3DW calculation, which differs from the srDWBA by accounting for the PCI to all orders of perturbation theory, provides a generally excellent description of the TDCS shapes and the angular positions of the observed peaks, outperforming the other two calculations in these regards. Clearly, for these symmetric low-energy kinematics, the inclusion of PCI is essential to accurately describe the physics of the collisions. Significant discrepancies between the experimental data and the sr3DW are, however, evident at the two smallest values of θ_1 and for small values of θ_2 at large θ_1 values. All three calculations predict the relative strengths of transitions to the two Kr^+ $4p^5$ states relative to the Kr^+ $4s$ state rather well, with the sr3DW method giving the best overall results.

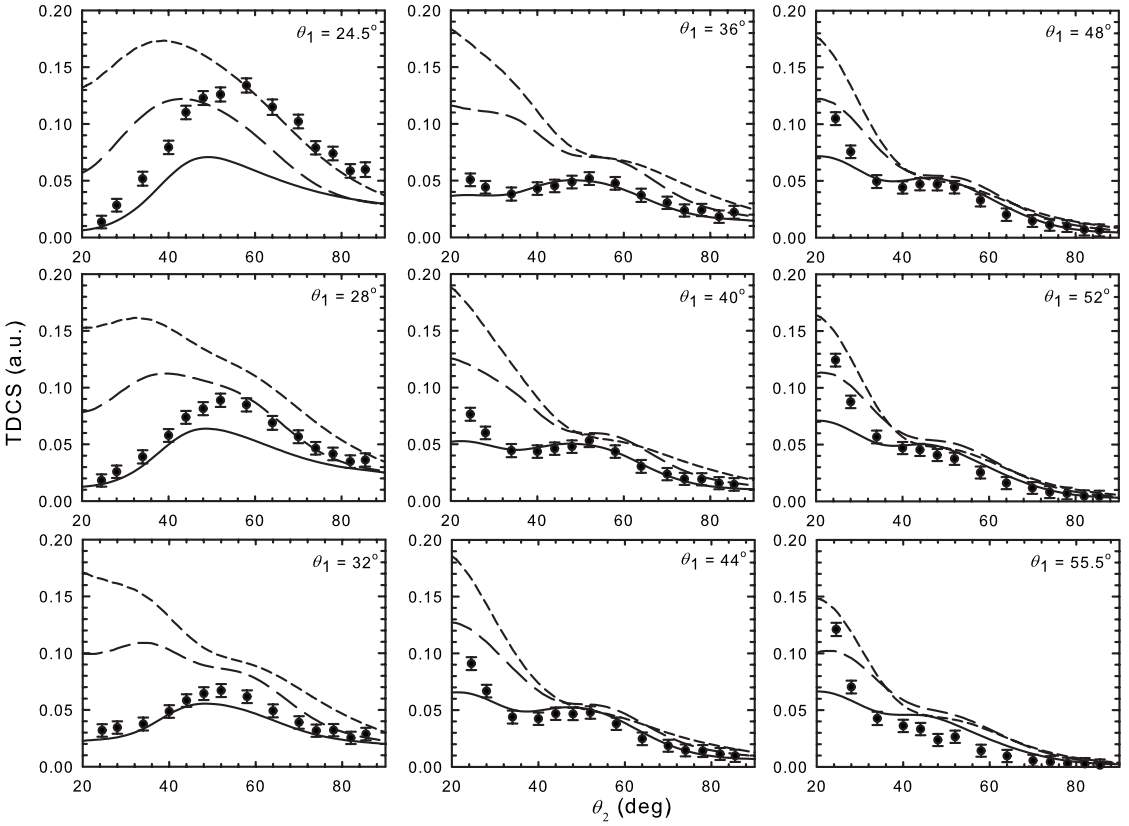

FIG. 4. TDCS for transitions to the Kr^+ $4p^5\ ^2P_{3/2}$ ion state. The incident beam energy E_0 is 114.3 eV, and the average energies $\bar{E}_1$ and $\bar{E}_2$, respectively, of the two outgoing electrons are 50.2 eV. Theory as in Fig. 3.

Figure 6 shows branching ratio data for the krypton, comprising the ratio of cross sections for transitions leading to the $^2P_{3/2}$ state relative to those leading to the $^2P_{1/2}$ state. Purely on the basis of the relative number of projection states m_j in the *LS*-coupling scheme and neglecting kinematic effects (see later), a value of 2 would be expected. However, deviations from *LS* coupling, which progressively increase with increasing atomic number Z of the target, lead to deviations from this value. Such deviations are largely attributable to bound-state effects, as differences between the radial wave functions describing the $^2P_{3/2}$ and $^2P_{1/2}$ ion states (which are identical in the nonrelativistic limit) increase as Z (and the fine-structure splitting) increases.

The experimental branching ratio shows discernible deviations from the value of 2 at all values of the scattering angles θ_1. By averaging over all values of θ_1 and θ_2 a branching ratio value of 2.14 ± 0.05 is obtained. The nrDWBA calculation (short-dashed line) predicts values very close to the value of 2.0 expected in the nonrelativistic limit. Small deviations from this value (barely discernible on the figure) do, however, occur on kinematic grounds. This is because, for the common value of impact energy E_0, the nrDWBA must account for the 0.67-eV fine-structure splitting through a corresponding difference in the average energies of the two scattered electrons between calculations for the $^2P_{1/2}$ and $^2P_{3/2}$ states. Both srDWBA (long-dashed line) and sr3DW calculations (solid line) describe the branching ratio data well, predicting an average value close to the experimentally determined value. Calculation of this quantity is apparently relatively insensitive to the inclusion of PCI through the sr3DW calculation. Moreover, the relatively small differences between the predictions of all three calculations for the branching ratio, in comparison to the large differences observed between the corresponding TDCSs, illustrates the insensitivity of this quantity to the magnitudes and shapes of the individual TDCSs.

The aim of the present work was to explore whether relativistic effects, unaccounted for in the theory, may have been the origin of disparities between theory and experiment in our earlier study of the electron-xenon system [1]. In order to do this, we performed the present electron-krypton experiments with identical energies for the scattered electrons. Figure 7 shows previously unpublished branching ratio results from our earlier xenon study. As expected, stronger deviations from a value of 2.0 are encountered for the xenon case due to the larger value of Z, with an average branching ratio value of 2.22 ± 0.05 obtained by averaging over all values of θ_1 and θ_2. The experimental results are compared to the same nrDWBA and sr3DW calculations as for the present krypton experiment. The small deviations from 2.0 for the nrDWBA (now clearly evident on the figure) are again due to the same kinematic effects described before, but this time enhanced due to the larger 1.3-eV (relative to 0.67 eV for krypton) fine-structure splitting. As anticipated, the sr3DW calculation provides a good description of the experimental branching ratio data, although not as good as for the electron-krypton case shown in Fig. 6. In particular, at $\theta_1 = 32°$ and $\theta_1 = 55.5°$, notwithstanding the superior statistics for this sys-

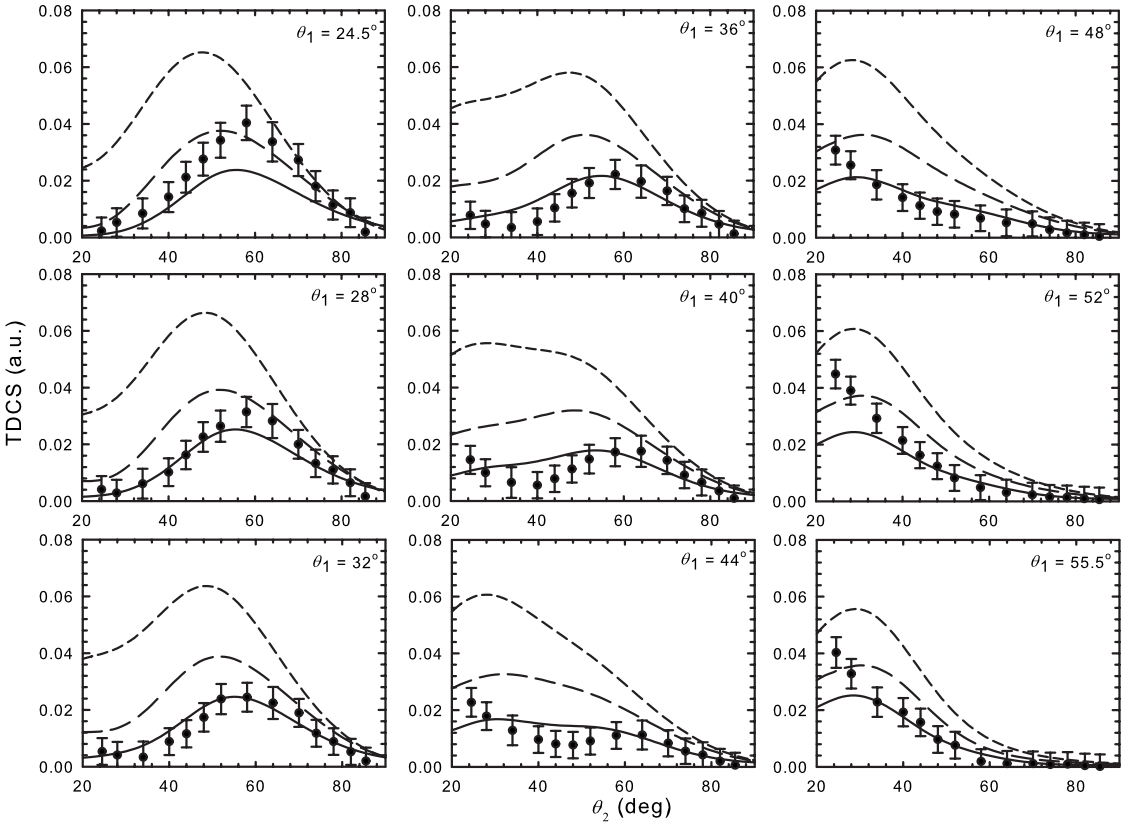

FIG. 5. TDCS for transitions to the Kr^+ $4s4p^6\,{}^2S_{1/2}$ ion state. The incident beam energy E_0 is 127.5 eV, and the average energies $\overline{E}_1$ and $\overline{E}_2$, respectively, of the two outgoing electrons are 50 eV. Theory as in Fig. 3.

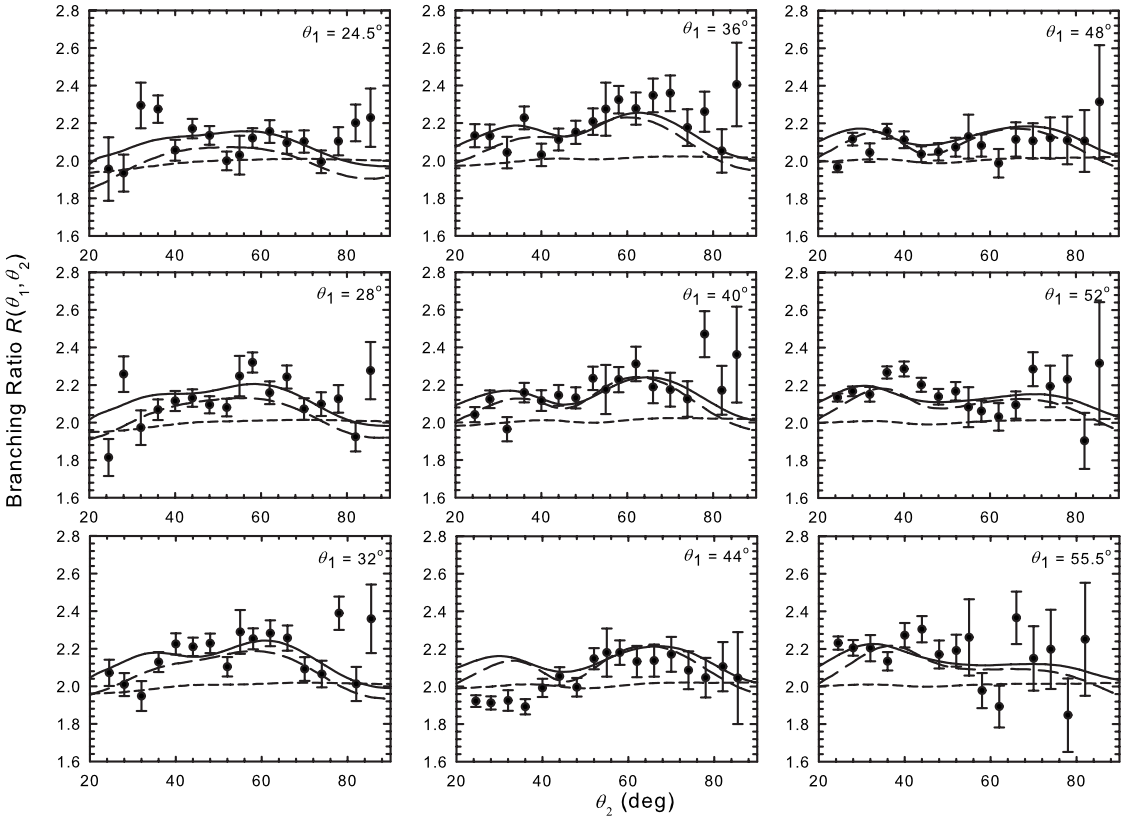

FIG. 6. Branching ratio $R(\theta_1,\theta_2)$ for krypton, calculated by dividing cross sections for transitions leading to the Kr^+ $4p^5\,{}^2P_{3/2}$ ion state by those for transitions leading to the Kr^+ $4p^5\,{}^2P_{1/2}$ ion state. Kinematics as described in Figs. 3 and 4. Theory as in Fig. 3.

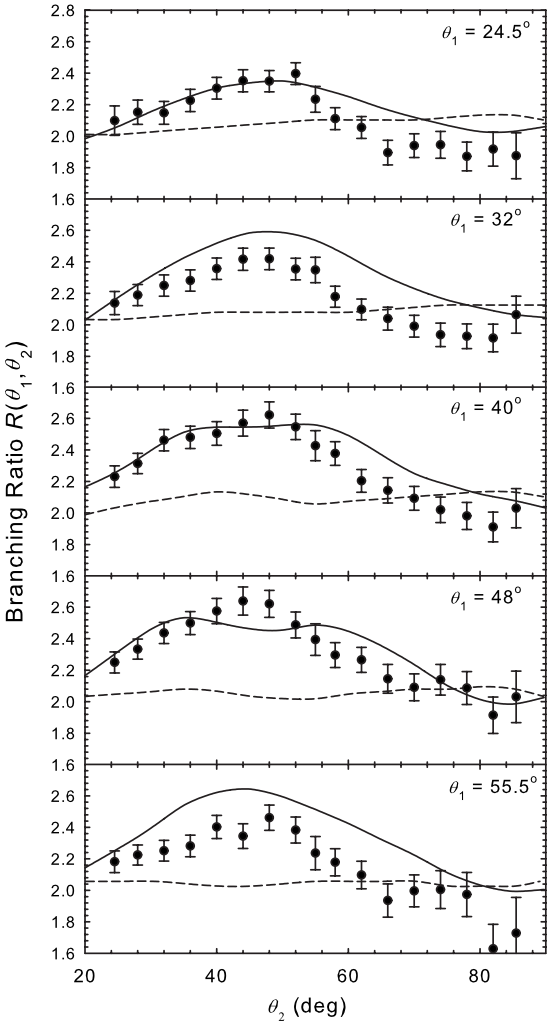

FIG. 7. Branching ratio $R(\theta_1, \theta_2)$ for xenon, calculated by dividing cross sections for transitions leading to the Xe^+ $5p^5\ ^2P_{3/2}$ ion state by those for transitions leading to the Xe^+ $5p^5\ ^2P_{1/2}$ ion state. The incident beam energy E_0 is 112 eV, and the average energies $\bar{E}_1$ and $\bar{E}_2$, respectively, of the two outgoing electrons are 50 eV. Theory as in Fig. 3.

tem, all theoretical predictions lie mostly outside the experimental error bars. This result suggests that in the case of the higher-Z xenon target a fully relativistic scattering theory may well be required to describe this quantity and corresponding TDCS data, which, as we previously explained [1], we were unable to reliably extract from the measurements at that time.

Figures 8 and 9 show spin asymmetries derived from experiment for the transitions leading to the Kr^+ $4p^5\ ^2P_{1/2}$ and $4p^5\ ^2P_{3/2}$ fine-structure levels, respectively. Errors ($\sim$6%) relating to uncertainties in the measured value of the beam polarization are not included in the experimental error bars, which are comprised of statistical and systematic components. The functions show oscillatory behavior, with the relation $A_{1/2}=A_{3/2}=0$, within error bars, being satisfied for the condition $\theta_1=\theta_2$ as required by parity conservation (for such symmetric energy and angle scattering and in the absence of spin selection for the incident and scattered electrons, the reaction, viewed in a mirror plane orientated perpendicular to the scattering plane, reverses the spin polarization of the incident beam, but leaves the final state unchanged; i.e., the spin asymmetry must be identically zero for parity to be conserved). Zero crossings are also seen to occur at other angles where $\theta_1 \neq \theta_2$; however, no such simple physical explanation is apparent to predict the angular coordinates where this occurs.

The experimental results are again compared to predictions from the three DWBA calculations. The srDWBA and sr3DW calculations both provide very good agreement with the experimental data with the exception of the largest scattering angle $\theta_1=55.5°$. In spite of considerable differences in their predictions for the individual TDCSs in Figs. 3–5, there is little difference evident between the predictions of the srDWBA and sr3DW calculations for this quantity involving the division of TDCS data. Slightly poorer predictions overall are provided by the nrDWBA calculation. Given that the asymmetry function is independent of the normalization factor K of Eq. (10) used to place the experimental TDCS data onto an absolute scale (it cancels out in the asymmetry quotient), the ability of all calculations to successfully predict the absolute magnitudes and signs of the asymmetry function over a broad range of kinematics is impressive.

For the case of a pure fine-structure effect (the nonrelativistic limit), $A_{1/2}=-2A_{3/2}$ and the branching ratio $R(\theta_1, \theta_2)=2.0$ [5]. Taken together, this implies that the value of the asymmetry function for transitions to unresolved fine-structure levels should be zero. In Fig. 10 we present data for transitions to the $4p$ state of the residual ion for which counts corresponding to the two fine-structure levels were first summed before the asymmetry was calculated. Within the error bars, zero values of asymmetry are indeed observed. By considering the reduced vertical scale of Fig. 10, any residual nonzero values for this function must be very small. We contrast this result with our earlier findings on xenon, for measurements performed under asymmetric scattering kinematics, where deviations from the above relations were clearly observed in the experimental results [28].

In light of the weaker signature of *bound-state* relativistic effects for krypton than for xenon, as presented by the branching ratio data previously discussed, it would seem reasonable to expect *continuum* relativistic effects, such as Mott scattering, would also be proportionally weaker for the electron-krypton than for the electron-xenon system. In order to test if Mott scattering may be playing a role in the present valence study, Fig. 11 presents spin asymmetry data for the Kr^+ $4s\ ^2S_{1/2}$ state. For this transition, due to the absence of fine structure, contributions to the spin-asymmetry function can only occur through continuum relativistic effects. No evidence of nonzero spin-asymmetry values is observed in the data, with deviations from zero consistent with expected statistical fluctuations. This null result suggests that the continuum spin-orbit effect, described through Mott scattering, is unlikely to influence the spin-asymmetry functions for the more weakly bound $^2P_{1/2}$ and $^2P_{3/2}$ ionic states under the present kinematics. This is reassuring as Mott scattering is not included in the present DWBA calculations, which employ identical distorted waves for spin-up and spin-down electrons and thus predict values of identically zero for Fig. 11.

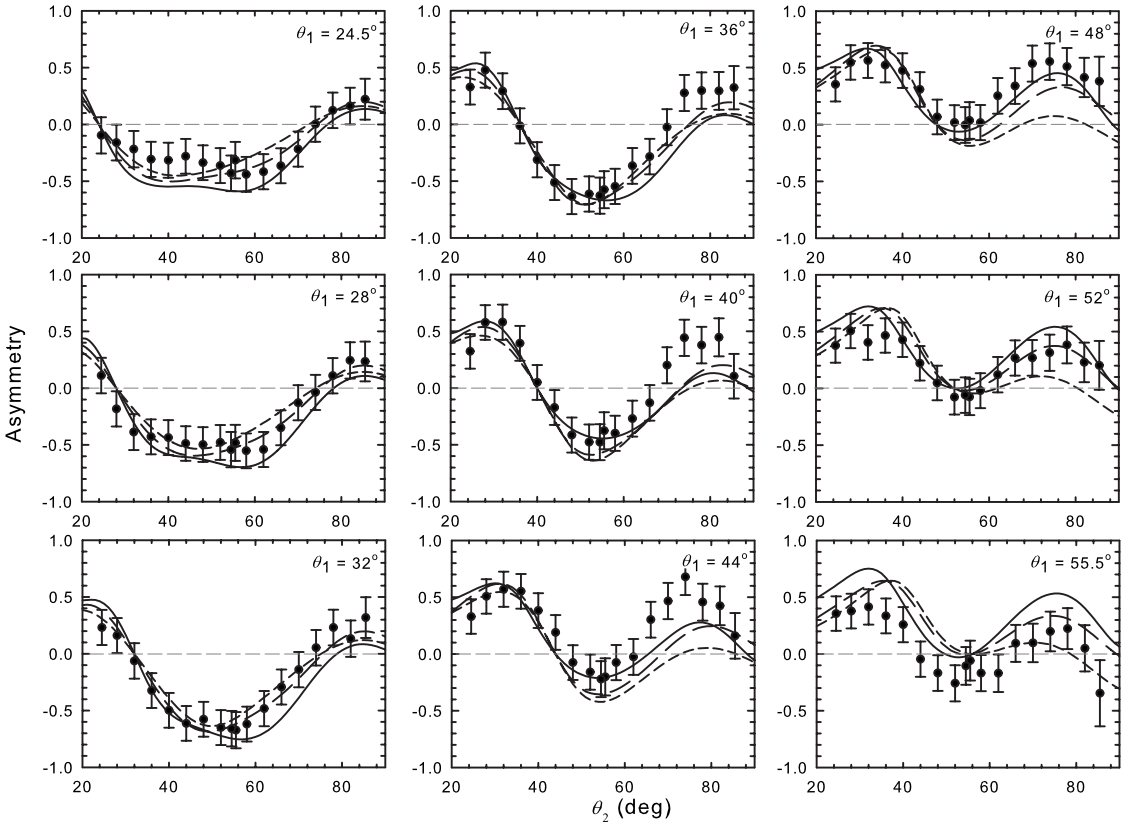

FIG. 8. Spin asymmetries for transitions leading to the Kr^+ $4p^5\,{}^2P_{1/2}$ ion state. Electron energies and theory as in Fig. 3 caption.

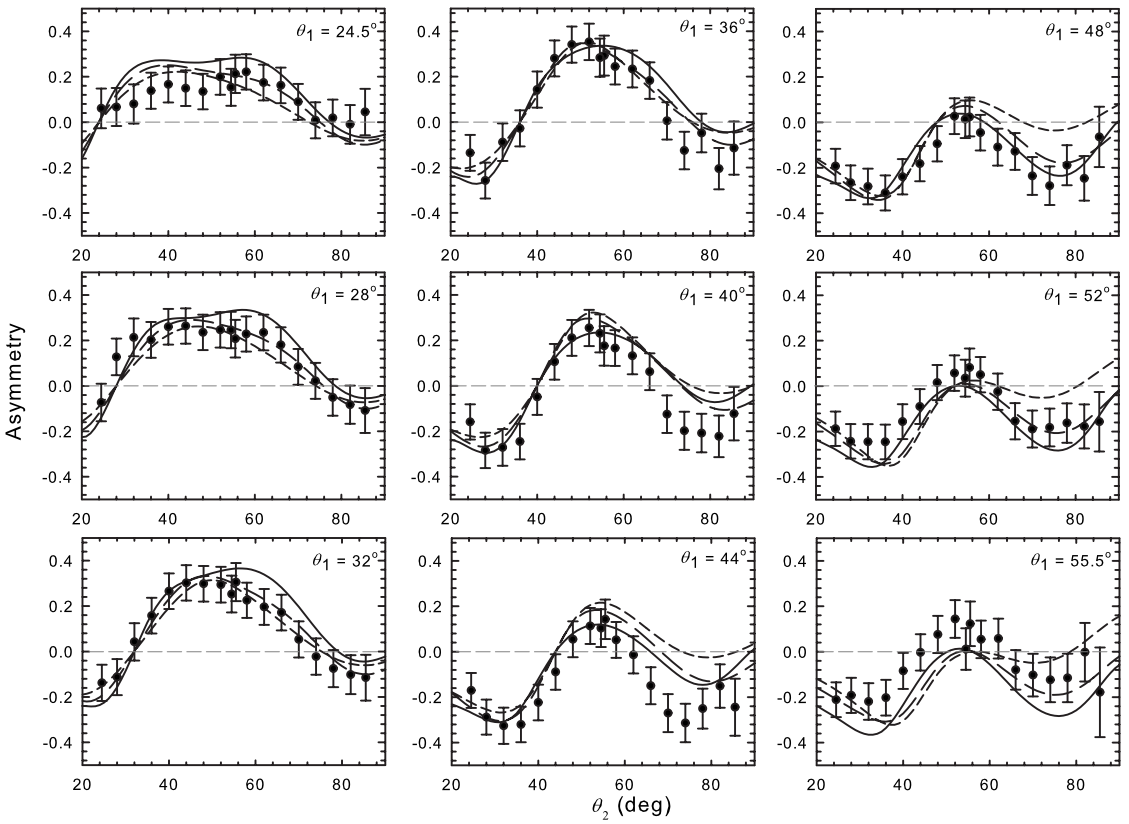

FIG. 9. Spin asymmetries for transitions leading to the Kr^+ $4p^5\,{}^2P_{3/2}$ ion state. Electron energies as in Fig. 4 caption and theory as in Fig. 3 caption.

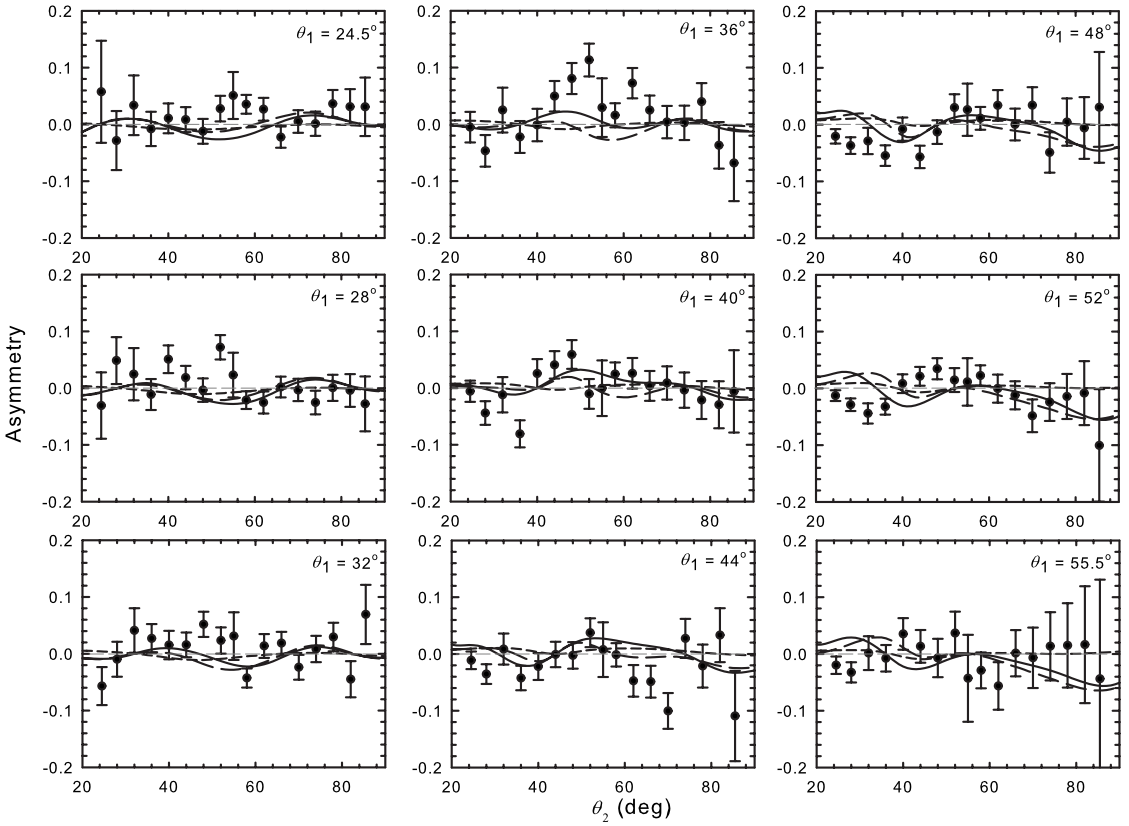

FIG. 10. Asymmetry for transitions to the Kr^+ $4p^5$ ion state for the case where the fine structure is unresolved. Kinematics as described in Figs. 3 and 4. Extremely small values for the asymmetry suggest the fine-structure-effect model, formulated in the nonrelativistic limit, provides an accurate physical picture of the mechanism underlying the measured spin asymmetries. Theory as in Fig. 3.

V. CONCLUSIONS

We have presented experimental and theoretical results for the electron-impact-induced ionization of krypton atoms by polarized electrons in which the fine-structure levels of the residual ion are resolved. The purpose of the study was to gain insight into the mechanisms underpinning the ionization of large-Z atoms by performing measurements with a high level of state specificity. Relative triple differential cross sections, spin asymmetries, and branching ratios are presented. The experimental TDCS data set is experimentally cross normalized, meaning that it is related to theory by a single common normalization constant over its entire kinematic range and thereby provides a stringent test.

In order to assess the present state of theory, identify areas of potential improvement, and gain insight into the contributions from different physical processes, the experimentally derived data are compared to three different calculations, each employing a different set of approximations. A comparison of the experimental TDCS data (Figs. 3–5) with the nrDWBA and srDWBA calculations shows that the distorted-wave Born approximation approach is extremely sensitive to the inclusion of relativistic effects in the description of the bound-state orbital of the active electron and to the use of relativistic distorting potentials in the calculation of the continuum electron wave functions. An equally dramatic sensitivity of the TDCSs to the inclusion of PCI is observed when comparing the srDWBA with the sr3DW calculation, with the former calculation not including this physical effect. The sr3DW calculation, which includes both relativistic and PCI effects, clearly provides the best description of the experimental data and is very successful in describing the shape and relative intensities of the TDCS across the broad range of kinematics covered by the present measurement.

The branching ratio is a quantity which can be directly compared to theory without normalization. For the krypton results of Fig. 6, excellent agreement is observed between the srDWBA and sr3DW calculations and experiment. For the xenon data presented in Fig. 7, notwithstanding the improved statistics in that case, the degree of agreement between the sr3DW and experiment is inferior to that achieved for krypton. This is perhaps indicative of the need for a more rigorous treatment of relativistic effects for higher-Z atoms. In both figures, as expected, the completely nonrelativistic nrDWBA calculation poorly describes the data.

The spin asymmetries (Figs. 8–11) are also quantities which can be directly compared to theory without normalization. All calculations provide a good description of the experimental data, with the srDWBA and sr3DW slightly outperforming the nrDWBA calculation. Indeed, both the srDWBA and sr3DW are spectacularly successful is describing the experimental data in both magnitude and sign. In stark contrast to the TDCS, the calculations show this quantity to be relatively insensitive to the description of relativistic and PCI effects. However, as nrDWBA, srDWBA, and sr3DW calculations all give zero spin-asymmetry values if

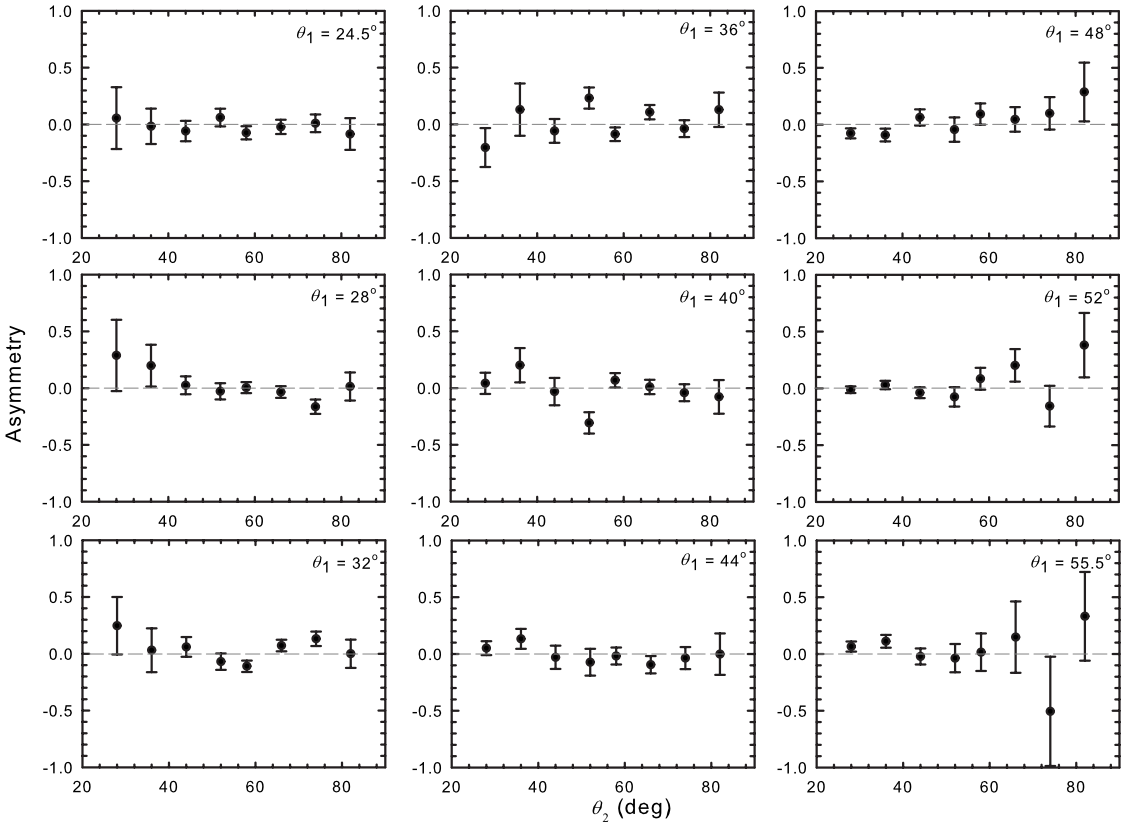

FIG. 11. Asymmetry data for ionizing transitions leading to the Kr^+ $4s\ ^2S_{1/2}$ ion state. Kinematics as in Fig. 5 caption. For this $L=0$ state, due to a lack of associated fine structure, spin asymmetries can only arise through continuum relativistic effects. The overall small magnitude of the measured asymmetry values suggests such effects are small for the present choice of target and kinematics.

exchange is neglected, the large nonzero values observed experimentally provide a sensitive test to the ability of the three theories to describe many-electron exchange processes. The close agreement observed between theory and experiment suggests that the present approach of adopting a local exchange approximation to account for exchange distortion in the calculations provides an excellent description of exchange processes under the present kinematics. Figure 11 shows spin asymmetries for the Kr^+ $4s\ ^2S_{1/2}$ state. Given the absence of fine structure, nonzero values of spin asymmetry can only occur through Mott scattering. The fact that a null result is observed, to within statistical accuracy, suggests that continuum spin-orbit effects do not significantly contribute to the spin asymmetries for the $4p^5\ ^2P_{1/2}$ and $4p^5\ ^2P_{3/2}$ ion states of Figs. 8 and 9.

The present sensitivity of the TDCS calculations to the partial inclusion of relativistic effects suggests that a fully relativistic DWBA, including an accurate treatment of PCI and exchange, might lead to substantially improved predictions. Such developments are planned by the authors. Furthermore, it is noted that the present DWBA calculations involve the evaluation of the first-order Born term only; the extent to which second-order Born effects might contribute has not been investigated in this study.

The main conclusion from the present study is the urgent need for experimental TDCS data on an absolute scale to more accurately assess the accuracy of different theoretical approaches. We have demonstrated that, through the DWBA approach, the inclusion of PCI, as well as a partial account of relativistic effects, leads to a substantially improved prediction for the shape of TDCS data under the present kinematics. However, without absolute experimental cross sections, how close the predicted TDCS *magnitudes* are to the true values cannot be assessed. To this end, we are planning to improve our experimental technique by employing the relative flow technique [29] to relate measured count rates for the ionization of heavy noble gases to those for ionization of helium under identical experimental conditions. With this approach, we can employ the convergent close coupling method [30], which can predict the TDCS for helium to very high accuracy, to place our TDCS data for heavy atoms onto an absolute scale.

ACKNOWLEDGMENTS

We gratefully acknowledge the assistance of the Australian Research Council under Grant No. DP0452553 (S.B. and J.L.) and the National Science Foundation under Grant No. PHY-0757749 (D.H.M.).

[1] S. Bellm, J. Lower, Z. Stegen, D. H. Madison, and H. P. Saha, Phys. Rev. A **77**, 032722 (2008).
[2] J. Kessler, Adv. At., Mol., Opt. Phys. **27**, 81 (1990).
[3] G. F. Hanne, Phys. Rep. **95**, 95 (1983).
[4] M. Dümmler, G. F. Hanne, and J. Kessler, J. Phys. B **28**, 2985 (1995).
[5] S. Jones, D. H. Madison, and G. F. Hanne, Phys. Rev. Lett. **72**, 2554 (1994).
[6] K. Bartschat and O. Zatsarinny, J. Phys. B **40**, F43 (2007).
[7] R. Panajotović, J. Lower, E. Weigold, A. Prideaux, and D. H. Madison, Phys. Rev. A **73**, 052701 (2006).
[8] G. F. Hanne, Can. J. Phys. **74**, 811 (1996).
[9] C. Mette, T. Simon, C. Herting, G. F. Hanne, and D. H. Madison, J. Phys. B **31**, 4689 (1998).
[10] A. Dorn, A. Elliott, X. Guo, J. Hurn, J. Lower, S. Mazevet, I. E. McCarthy, Y. Shen, and E. Weigold, J. Phys. B **30**, 4097 (1997).
[11] H. Müller and J. Kessler, J. Phys. B **27**, 5893 (1994).
[12] I. Fuss, R. Glass, I. E. McCarthy, A. Minchinton, and E. Weigold, J. Phys. B **14**, 3277 (1981).
[13] K. T. Leung and C. E. Brion, Chem. Phys. **82**, 87 (1983).
[14] R. Nicholson, S. W. Braidwood, I. E. McCarthy, E. Weigold, and M. J. Brunger, Phys. Rev. A **53**, 4205 (1996).
[15] I. E. McCarthy and E. Weigold, *Electron-Atom Collisions* (Cambridge University Press, Cambridge, England, 1995).
[16] P. Selles, J. Mazeau, and A. Huetz, J. Phys. B **23**, 2613 (1990).
[17] J. Rasch, M. Zitnik, L. Avaldi, C. T. Whelan, G. Stefani, R. Camilloni, R. J. Allan, and H. R. J. Walters, Phys. Rev. A **56**, 4644 (1997).
[18] S. J. Cavanagh, B. Lohmann, J. Rasch, C. T. Whelan, and H. R. J. Walters, Phys. Rev. A **60**, 2977 (1999).
[19] J. F. Williams, R. W. van Boeyen, and S. Samarin, Phys. Rev. A **71**, 052709 (2005).
[20] M. A. Haynes, B. Lohmann, A. Prideaux, and D. H. Madison, J. Phys. B **36**, 811 (2003).
[21] S. Mazevet, I. E. McCarthy, and E. Weigold, Phys. Rev. A **57**, 1881 (1998).
[22] J. B. Furness and I. E. McCarthy, J. Phys. B **6**, 2280 (1973).
[23] J. Lower, R. Panajotović, S. Bellm, and E. Weigold, Rev. Sci. Instrum. **78**, 111301 (2007).
[24] S. Bellm, J. Lower, E. Weigold, I. Bray, D. V. Fursa, K. Bartschat, A. L. Harris, and D. H. Madison, Phys. Rev. A **78**, 032710 (2008).
[25] J. Lower and E. Weigold, J. Phys. E **22**, 421 (1989).
[26] A. Prideaux and D. H. Madison, J. Phys. B **37**, 4423 (2004).
[27] A. Prideaux and D. H. Madison, Phys. Rev. A **67**, 052710 (2003).
[28] A. Dorn, A. Elliott, J. C. Lower, S. F. Mazevet, R. P. McEachran, I. E. McCarthy, and E. Weigold, J. Phys. B **31**, 547 (1998).
[29] S. K. Srivastava, A. Chutjian, and S. Trajmar, J. Chem. Phys. **63**, 2659 (1975).
[30] I. Bray and A. T. Stelbovics, Phys. Rev. A **46**, 6995 (1992).